

Article

Engineering the Quaternary Hydrotalcite-Derived Ce-Promoted Ni-Based Catalysts for Enhanced Low-Temperature CO₂ Hydrogenation into Methane

Yuxin Peng¹, Xin Xiao^{2,3,*} , Lei Song¹, Ning Wang⁴  and Wei Chu^{1,*}

¹ School of Chemical Engineering, Sichuan University, Chengdu 610065, China; pyx18908007922@163.com (Y.P.); songlei@scu.edu.cn (L.S.)

² College of Carbon Neutrality Future Technology, Sichuan University, Chengdu 610106, China

³ National Engineering Research Centre for Flue Gas Desulfurization, Chengdu 610065, China

⁴ College of Environmental and Energy Engineering, Beijing University of Technology, Beijing 100124, China; ning.wang.1@bjut.edu.cn

* Correspondence: xiaoxin93@scu.edu.cn (X.X.); chuwei1965@scu.edu.cn (W.C.)

Abstract: Ce-promoted NiMgAl mixed-oxide (NiCex-C, x = 0, 1, 5, 10) catalysts were prepared from the quaternary hydrotalcite precursors for CO₂ hydrogenation to methane. By engineering the Ce contents, NiCe5-C showed its prior catalytic performance in low-temperature CO₂ hydrogenation, being about three times higher than that of the Ce-free NiCe0-C catalyst (turnover frequency of NiCe5-C and NiCe0-C: 11.9 h⁻¹ vs. 3.9 h⁻¹ @ 225 °C). With extensive characterization, it was found that Ce dopants promoted the reduction of NiO by adjusting the interaction between Ni and Mg(Ce)AlO_x support. The highest ratio of surface Ni⁰/(Ni²⁺ + Ni⁰) was obtained over NiCe5-C. Meanwhile, the surface basicity was tailored with Ce dopants. The strongest medium-strength basicity and highest capacity of CO₂ adsorption was achieved on NiCe5-C with 5 wt.% Ce content. The TOF tests indicated a good correlation with medium-strength basicity over the NiCex-C samples. The results showed that the high medium-strength and Ce-promoted surface Ni⁰ species endows the enhanced low-temperature catalytic performance in CO₂ hydrogenation to methane.

Keywords: Ce dopants; Ni-based catalyst; CO₂ methanation; lower temperature performance; quaternary hydrotalcites



Citation: Peng, Y.; Xiao, X.; Song, L.; Wang, N.; Chu, W. Engineering the Quaternary Hydrotalcite-Derived Ce-Promoted Ni-Based Catalysts for Enhanced Low-Temperature CO₂ Hydrogenation into Methane. *Materials* **2023**, *16*, 4642. <https://doi.org/10.3390/ma16134642>

Academic Editor: Barbara Pawelec

Received: 15 May 2023

Revised: 15 June 2023

Accepted: 23 June 2023

Published: 27 June 2023



Copyright: © 2023 by the authors. Licensee MDPI, Basel, Switzerland. This article is an open access article distributed under the terms and conditions of the Creative Commons Attribution (CC BY) license (<https://creativecommons.org/licenses/by/4.0/>).

1. Introduction

Recently, CO₂ reduction and recycling has become one of the most researched hotspots in neutral carbon economics due to the serious impact on global climate change led by growing CO₂ emissions [1,2]. To mitigate the increasing anthropogenic CO₂, methods like CO₂ capture, utilization, and storage (CCUS) had been engaged [3]. Among these methods, the conversion of CO₂ with “green hydrogen” (hydrogen originates from sustainable energy, like wind, solar, etc.) into synthetic natural gas (SNG) has been considered as one of the most promising and practical approaches for CO₂ utilization [4,5]. SNG, as a high value-added fuel product, plays a vital role as a raw material in the synthesis of syngas and many chemical products [6]. CO₂ hydrogenation to the SNG reaction, which was also called the Sabatier reaction, displayed a great potential in the “Power to Gas” process [7]. However, this reaction went through an eight-electron process for CO₂ reduction into methane, which suffered significant kinetic limitations [8]. To solve this puzzle, a catalytic material that could achieve high reaction rates was required. Ni-based catalysts with high reaction activity and low-cost aroused extensive interest of researchers [9]. Meanwhile, in practical application, Ni-based catalysts always suffered from inferior activity at low temperatures [10]. Compared to the CO₂ methanation reaction in a higher temperature, the low-temperature CO₂ methanation showed advantages in

two different aspects: (I) The competitive reaction, like the reverse water gas shift (RWGS) reaction, could be effectively reduced at low temperatures, and the catalysts obtained a high CH₄ selectivity. (II) The sintering and carbon deposition problems of the catalyst usually occurred at high temperatures; the low temperature condition was conducive to the catalyst's stability [11–13]. Therefore, improving the low temperature activity of Ni-based catalysts is a current research hotspot [14].

The catalytic activity of Ni-based catalysts is usually related to the basic nature of the catalyst carrier and the preparation method [15]. Compared with Ni/ γ -Al₂O₃ catalysts prepared by impregnation, Ni-Al hydrotalcite catalysts prepared by co-precipitation could contain a higher content of well-dispersed Ni nanoparticles with more reducible Ni species [16]. Hydrotalcite (HT) was a kind of natural or synthetic ordered material which consisted of positively charged two-dimensional sheets of mixed hydroxides and charge-compensating anions placed between the layers [17]. They were expressed as [M²⁺_{1-x}M³⁺_x(OH)₂](Aⁿ⁻)_{x/n} · mH₂O (M²⁺ and M³⁺ were divalent and trivalent metals, respectively; x was the mole ratio of M³⁺/(M²⁺ + M³⁺), Aⁿ⁻ was the interlayer anion) [7]. The unique supramolecular structure provided great potential to disperse and tune active sites at the atomic scale [18]. Introducing a proportion of alkaline elements into the HT precursor could obtain a tunable alkaline site structure and promote CO₂ adsorption, which would benefit the CO₂-involving reaction. For instance, the addition of the Mg element could improve the catalyst's basic properties, result in the increase of the CO₂ adsorption capacity [19]. Moreover, small-size and heat-stable metal nanoparticles were highly dispersed on the calcined HT precursor surface after reduction; thus, the catalyst stability and reducibility would get enhanced [10]. For example, Guo et al. [20] synthesized that the hydrotalcite-derived NiMgAl catalyst exhibited excellent catalytic activity with a CO₂ conversion of 91.8% at 250 °C. Therefore, it was a promising approach by fabricating the alkaline-assisted hydrotalcite-derived materials to obtain the efficient low-temperature catalyst for CO₂ methanation.

However, traditional NiMgAl catalysts derived from hydrotalcite also suffered from strong metal-support interactions [21]; thus, a long-time H₂ reduction process was needed to enhance reducibility. To overcome this drawback, quite a few reports were found to introduce a second metal (such as Mn, La, and Y) to replace the partial Mg element [22,23], thereby regulating the metal-support interaction. As reported by our group [11], the doping of the Mn element could efficiently regulate the Ni and Mg(Mn)AlO_x interaction, surface content of Ni⁰ species, and basic property. Dominik Wierzbicki et al. [24] supposed La could soften the interaction between Ni and the HT matrix and lead to the increase of Ni-species reducibility [25]. Sun et al. found the incorporation of the 0.4 wt.% Y strongly decreased the metallic nickel particle size and increased the medium-strength basic sites.

Besides the Mn, La, Y species, CeO₂, as a rare earth oxide, had also been a very attractive promoter for CO₂ methanation due to its extraordinary ability to enhance metal dispersion, as well as the thermal stability of the support [26,27]. Moreover, the rare earth metal element Ce owns redox properties [28]. During the reaction, Ce metal ions are reduced to produce oxygen vacancies, which are the sites of dissociation and activation of CO₂ [28,29]. Radosław Debek et al. [30] reported CeO₂ had a promoting effect on increasing the surface basicity of the catalyst, which was attributed to its high mobile oxygen capacity and redox activity. The process of reducing CO₂ to CO was the rate-determining step of CO₂ methanation. In addition, the oxygen vacancy provided by the CeO₂ could create an additional driving force for this process in the reducing atmosphere [31]. Zhang et al. [32] considered that Ce³⁺ cations located in the AlCeO₃ solid solution could greatly promote the adsorption and activation of CO₂ and facilitate the formation of the intermediate; therefore, the CO₂ conversion was significantly accelerated at 200 °C. In the dry reforming of methane (DRM) reaction, Radosław Debek et al. [17,33] incorporated Ce species into the NiMgAl catalysts, which was found to promote the nickel species' reducibility and introduce new strong oxygen species (low coordinated) and more medium-strength basic sites (Lewis acid-base pairs).

Furthermore, a recent literature compared different Ni content (10.3, 16.2, 27.3, 36.8, 42.5 wt.%) on the performance of hydrotalcite-derived catalysts, and the optimum Ni content was 42.5 wt.%. This result confirmed that higher amounts of Ni introduced led to smaller crystallites, better reducibility, and CO₂ adsorption capacity of the catalysts. H₂-TPR proved the Ni and hydrotalcite matrix interaction weakened with the increasing Ni contents, which had a positive effect on the catalytic activity [34]. However, according to our knowledge, quaternary hydrotalcite-derived Ce-containing Ni-Ce catalysts had not been widely used in CO₂ methanation. Herein, our goal was to study the structure–performance relationships between them. We prepared a series of Ce-promoted Ni/MgAlOx catalysts through the co-precipitation method in this study. The low-temperature catalytic performance was investigated by varying Ce content from 0, 1, 5 to 10 wt.%. The optimal sample displayed superior CO₂ methanation activity with 80% CO₂ conversion at a low temperature of 250 °C, and the CH₄ selectivity was close to 100%. Meanwhile, the CO₂ conversion (91.7%) was not deactivated upon 80 h of operation at 300 °C. Extensive characterization methods (XRD, BET, ICP SEM, TEM, XPS, H₂-TPR, CO₂-TPD) were used to deeply analyze the promoting effect of Ce on influencing the catalyst structure, morphology, surface properties, metal-support interaction, and performances during CO₂ methanation.

2. Experimental

2.1. Catalyst Synthesis

All of the hydrotalcite precursors were prepared by the co-precipitation method. Ni content was kept at 40 wt.% and the Mg/Al molar ratio was fixed at 1 in all samples, while the loading of Ce varied from 0, 1, 5 to 10 wt.%. Firstly, the mixture of Ni(NO₃)₂·6H₂O, Mg(NO₃)₂·6H₂O, Al(NO₃)₃·9H₂O, and Ce(NO₃)₃·6H₂O was dissolved in deionized water to form a solution at 0.4 M. Then, the mixed nitrate solution was added dropwise into a flask containing 280 mL sodium carbonate solution (0.25 M) at 60 °C under vigorous stirring, while at the same time, keeping the slurry pH at 9.5–10 by adding the sodium hydroxide solution (1 M). After co-precipitation, the slurry was vigorously stirred at 60 °C for 1 h and then aged for 18 h at 60 °C. The solid product was obtained by filtration, washed with deionized water three times, dried at 60 °C overnight, and named as NiCe0-HT (without Ce) or NiCex-HT (x = 1, 5, 10). Finally, the obtained hydrotalcite precursors were calcined at 500 °C for 4 h and labeled as NiCex-C (x = 0, 1, 5, 10).

2.2. Catalytic Experiments

The CO₂ methanation reaction was performed in a miniature fixed-bed reactor (Xingtianyu, Chengdu, China) at atmospheric pressure. A total of 200 mg of the catalyst (40–60 mesh) mixed with 500 mg of quartz sand were placed in the quartz tube (inner diameter of 6mm and a length of 40 cm). Prior to the catalyst evaluation, the catalysts were reduced under 30 mL/min H₂ at 700 °C for 2 h. After reduction, the catalyst bed was cooled down in the N₂ atmosphere to 180 °C; then, the mixture of 40 mL/min H₂ and 10 mL/min CO₂ (H₂:CO₂ = 4:1, GHSV = 15,000 mL/g/h) was introduced into the reactor. The catalytic test was carried out in the temperature range of 200–350 °C at a temperature interval of 25 °C. The gas products were analyzed by an online SP-7890 gas chromatograph (Lunan Ruihong, Zaozhuang, China) equipped with a thermal conductivity detector (TCD, Xian quan, Tianjing, China) (fitted with a TDX01 column). The conversions of CO₂ (X_{CO_2}) and the selectivity of CH₄ (S_{CH_4}) were calculated by the following equations [35]:

$$X_{\text{CO}_2} = \left(\frac{F_{\text{CO}_2,\text{in}} - F_{\text{CO}_2,\text{out}}}{F_{\text{CO}_2,\text{in}}} \right) \times 100\% \quad (1)$$

$$S_{\text{CH}_4} = \left(\frac{F_{\text{CH}_4,\text{out}}}{F_{\text{CO}_2,\text{in}} - F_{\text{CO}_2,\text{out}}} \right) \times 100\% \quad (2)$$

where “ $F_{\text{CO}_2,\text{in}}$ ” and “ $F_{\text{CO}_2,\text{out}}$ ” refer to the inlet CO₂ gas flow and the outlet CO₂ gas flow, respectively, and “ $F_{\text{CH}_4,\text{out}}$ ” refers to the outlet CH₄ gas flow, mL/min.

The equations of the CO₂ conversion rate (R_{CO_2} , $\mu\text{molCO}_2/(\text{g}_{\text{cat}}\cdot\text{s})$) and turnover frequency (TOF , h^{-1}) are as follows [36,37].

$$R_{\text{CO}_2} = \frac{F_{\text{CO}_2,\text{in}} \times X_{\text{CO}_2}}{m \times V_m} \quad (3)$$

where V_m represents the gas molar volume of 22.4 L/mol under standard conditions, X_{CO_2} refers to the conversion of CO₂ at 225 °C ($X_{\text{CO}_2} < 15\%$), and m denotes the quantity of the catalyst (g) [11,38]

$$\text{TOF} = \frac{F_{\text{CO}_2,\text{in}} \times \delta}{N_{\text{surface}} \times V_m} \quad (4)$$

$$N_{\text{surface}} = N_{\text{total}} \times D \quad (5)$$

where δ represents the methane yield and N_{surface} represents the molar amount of nickel atoms located on the catalyst surface, which is calculated by the nickel dispersion equation (D , %) based on the size of the Ni nanoparticles after reduction (TEM result).

The apparent activation energy of the catalyst was measured according to the Arrhenius equation:

$$\ln k = \ln k_0 - \frac{E_a}{RT} \quad (6)$$

where k is the reaction rate, k_0 is the pre-exponential factor, E_a is the apparent activation energy of the reaction, R is the gas reaction constant (8.314 J/(mol·K)), and T is the reaction temperature. The experimental conditions were carefully selected to obtain the catalytic data with CO₂ conversion below 15% for the activation energy calculation, which effectively excluded the influence of internal and external diffusion [38].

2.3. Characterization of Catalysts

A powder X-ray diffraction (XRD) measurement was performed on a Rigaku Ultima IV (Japan) device equipped with a copper-based anode (Cu K α radiation, $\lambda = 0.154$ nm). The instrument settings were 35 kV \times 30 mA. It operated in the 2θ range from 5° to 85° with the scanning speed of 2°·min⁻¹ to identify the crystal phase and morphology of the sample.

The hydrogen temperature-programmed reduction (H₂-TPR) measurement was performed on a TP-5080 instrument equipped with a TCD detector (Xianquan, Tianjing, China) to investigate the reduction performance of the catalyst. Firstly, 50 mg of the catalyst was placed in the quartz tube, then 30 mL/min N₂ was put into the instrument for 1 h at 200 °C to remove the physical adsorbed impurities on the catalyst's surface. After cooling down to 50 °C under argon, 28 mL/min 10% H₂/N₂ mixture was introduced to reduce the catalyst, and the system was kept at 50 °C for 40 min until the baseline was stable. Then, the reactor temperature was linearly increased from 50 °C to 800 °C at a heating rate of 5 °C/min.

The carbon dioxide temperature-programmed desorption (CO₂-TPD) was carried out on an Auto Chem II 2920 apparatus to determine the basic sites on the catalyst surface. Firstly, 0.1 g catalyst was placed in the quartz tube, and 30 mL/min H₂/Ar was put into the device for 10 min at room temperature to remove the residual gas in the tube. Then, the catalyst was reduced in H₂/Ar at 700 °C for 2 h. After that, the sample was cooled down to 50 °C in the N₂ atmosphere. After CO₂ adsorption of the catalyst for 1 h, N₂ was put into the system to remove the remaining CO₂ in the gas phase and the physically adsorbed CO₂ on the catalyst surface. Finally, the system was heated from 50 °C to 800 °C at a linear heating rate of 10 °C/min to desorb the chemisorbed CO₂ on the catalyst surface.

The N₂ adsorption-desorption analysis was carried out on the ASAP 2020 (Micrometrics, Norcross, GA, USA) analyzer at -196 °C. All samples were degassed at 300 °C for 6 h before the analysis to desorb contaminants and moisture. The specific surface area was characterized by an adsorption isotherm according to the multiple Brunauer-Emmett-Teller (BET) equation. The pore size distribution and average pore diameter were determined by the Barrett-Joyner-Halenda (BJH) model. Inductively coupled plasma optical emission spec-

trometer (ICP-OES, Agilent, Santa Clara, CA, USA) was carried out by Agilent 5110(OES) equipment to conduct elemental analysis of the catalysts.

X-ray photoelectron spectroscopy (XPS) measurements were performed over a K-Alpha spectrometer (Thermo Scientific, Waltham, MA, USA) equipped with a Monochromated Al K α X-ray source ($h\nu = 1486.6$ eV, 12 kV, 6 mA). The binding energy standard was C1s = 284.80 eV.

A ZEISS Sigma 30 scanning electron microscope (SEM) was used to study the morphology of the catalyst precursor. The acceleration voltage was 3 kV, and the magnification was 5 W and 10 W times. Moreover, the morphology, the particle size distribution, and the lattice spacing of the calcined and reduced catalysts were characterized by field emission transmission electron microscopy (TEM), which was performed on an FEI Tecnai G2 F20 instrument (USA) with an acceleration voltage of 200 kV.

3. Results and Discussion

3.1. Texture Characteristics of the NiCex-C Catalysts

Figure 1a showed the XRD diffraction profiles of precursors with various Ce contents. Distinct diffraction peaks were observed at $2\theta \sim 11^\circ$, $\sim 22^\circ$, $\sim 34^\circ$, $\sim 38^\circ$, $\sim 46^\circ$, $\sim 60^\circ$, and $\sim 61^\circ$ for all the samples, which belonged to (003), (006), (012), (015), (018), (110), and (113) of the hydrotalcite characteristic structure (JCPDS-22-0700) [11]. In particular, compared with the Ce-free sample, obviously weaker and wider diffraction peaks were observed in other Ce-containing samples. These results indicated that the Ce doping could influence the crystallinity of the sample and disturb the hydrotalcite plate layer structure [39]. Figure 1b showed the XRD spectrum of samples after calcination at 500 °C for 4 h, and it could be found that the disappearance of all the diffraction peaks corresponded to hydrotalcite-like structures. The peaks at $2\theta = 37.3^\circ$, 43.3° , 62.9° , and 75.5° were corresponded to (111), (200), (220), and (311) crystal planes of NiO, respectively (JCPDS-47-1049) [40]. After adding the Ce element, the intensity of these characteristic peaks in the samples decreased significantly. Meanwhile, well-crystallized CeO₂ could be observed after calcination. The peaks at 28.5° , 33.0° , 47.4° , and 56.3° were indexed to (111), (200), (220), and (311) crystal planes of CeO₂ (JCPDS-34-0394) [41]. In special, the diffraction peaks corresponding to MgO and Al₂O₃ were absent. The Al and Mg species may form as an amorphous structure or as a part of the MgAl₂O₄ spinel, whose diffraction peaks were overlapped by the periclase [11,42].

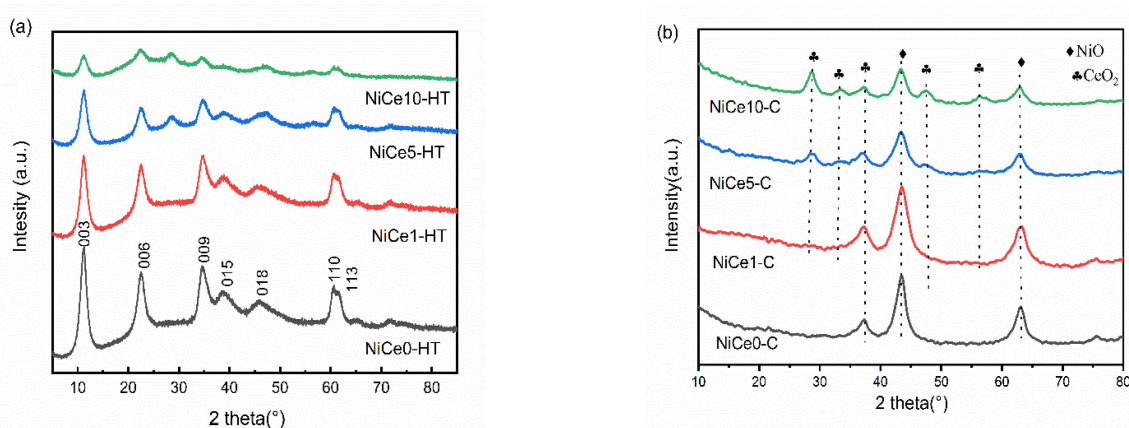


Figure 1. XRD patterns of the hydrotalcite-like precursors NiCex-HT (a) and the mixed oxides NiCex-C (b).

Texture properties of the NiCex-C catalysts were investigated by N₂ adsorption-desorption analysis. As presented in Figure 2a, according to the IUPAC classification, all the samples displayed an IV N₂ adsorption-desorption isotherm ($P/P_0 > 0.4$) with H2 hysteresis loops, corresponding to the typical features of mesoporous structures [3]. The pores might originate from the stack of the 2D structure of HT, which was conducive to the

adsorption and activation of active gases, promoting the mass transmission process [43]. As shown in Figure 2b, all samples featured typical mesoporous structures with narrow pore size distributions, concentrated from 2 to 10 nm. In addition, the detailed textural properties of the NiCex-C catalysts were listed in Table 1. All the catalysts derived from hydrotalcite-like compounds displayed large specific surface areas ($>100 \text{ m}^2/\text{g}$), which allowed for a better dispersion of surface nickel species [44]. The mean pore diameters of the catalysts were all slightly decreased after the introduction of the Ce element, mainly due to the Ce species on the external porous surface of the hydrotalcite crystallites, causing the blockage of partial smaller mesoporous [45]. On the other hand, there was no significant difference in the average pore volume among all samples.

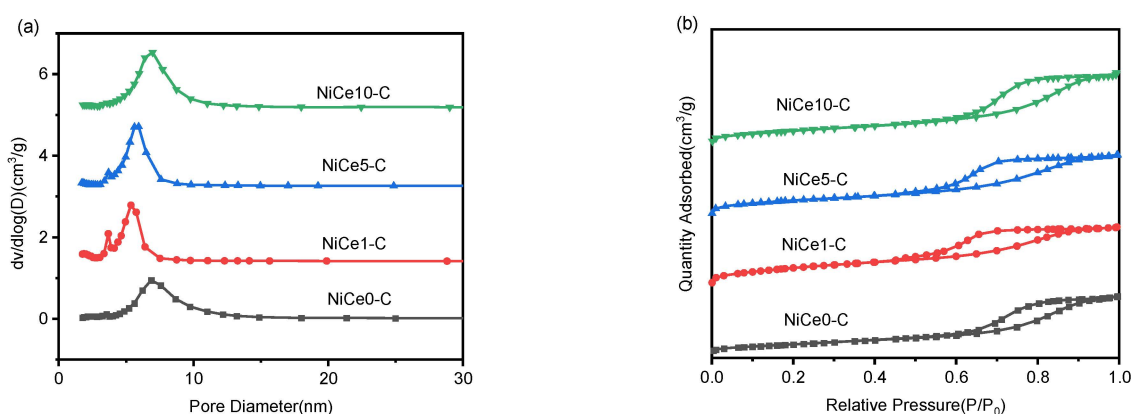


Figure 2. N_2 adsorption-desorption isotherms (a) and distributions of the pore size of the NiCex-C catalysts (b).

Table 1. Detailed information about the textural properties of the NiCex-C catalysts.

Sample	S_{BET}^a (m^2/g)	V_p^b (cm^3/g)	D_p^c (nm)	Ni ^d %	Ce ^e %	Mg/Al ^f
NiCe0-C	127.7	0.24	6.41	44.5	0.0	1.5
NiCe1-C	215.0	0.25	6.25	40.5	0.79	1.5
NiCe5-C	176.9	0.26	5.24	40.1	4.07	1.5
NiCe10-C	169.0	0.29	4.37	42.3	8.70	1.4

^a BET specific surface area. ^b Calculated from the adsorption amount of N_2 at a relative pressure (P/P_0) of 0.98. ^c BJH Desorption average pore diameter. ^{d-f} Determined by ICP-OES measurement. Actual Ni, Ce content, and Mg/Al.

3.2. Morphological Study and the Particle Size Analysis

The SEM images of the NiCe0-HT sample with the magnification of 10W and 5W were shown in Figures 3a and 3c, respectively. It was found that the NiCe0-HT exhibited platelet-like crystals that were aggregated as rosettes, referring to the typical characteristic for the hydrotalcite structure [46]. However, the morphology of the Ce-loading sample (NiCe5-HT) was found unchanged (Figure 3b,d). It further indicated that the hydrotalcite-like structure could be well-generated, which was identical to the XRD results.

TEM measurements were used to observe the state of all the calcined and reduced NiCex-C catalysts. As shown in Figure 4, the dark spots were ascribed to the Ni nanoparticles dispersed on the frame of the mixed metal oxide. For all samples, the layered structure of the hydrotalcite precursors partially collapsed after calcination. The morphology and the Ni particle dispersion were varied due to the introduction of different Ce contents. For the Ce-containing catalysts, Ni nanoparticles dispersed evenly on the catalyst surface. While large clusters of Ni particles were observed on the surface of the NiCe0-C catalyst, the dispersion of Ni nanoparticles was poor. In addition, the well-defined lattice fringes assigned to the face-centered cubic Ni (111) surface were observed in HRTEM images for all samples, with an average lattice spacing of 0.2 nm [4].

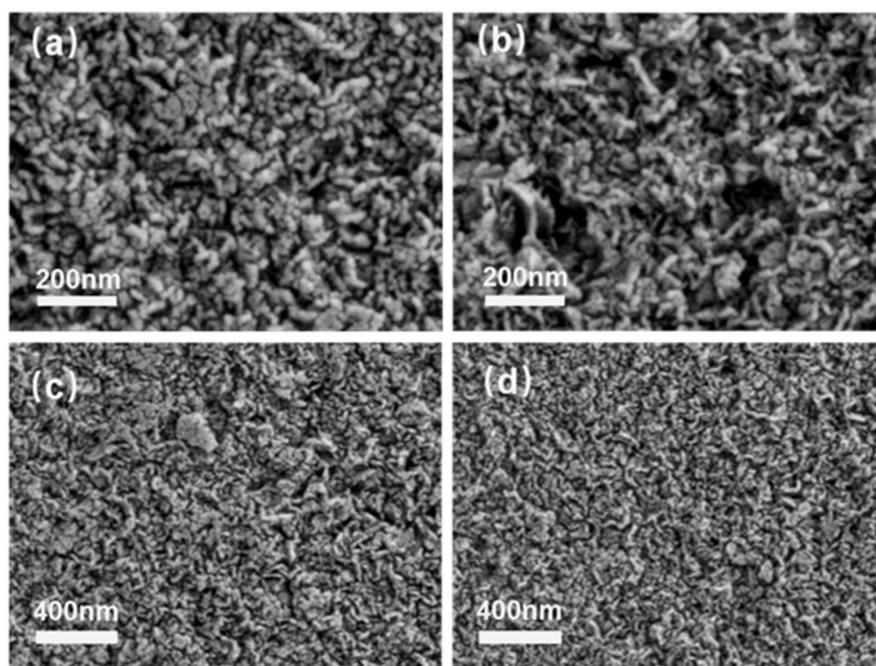


Figure 3. SEM images of (a,c) NiCe0-HT, (b,d) NiCe5-HT.

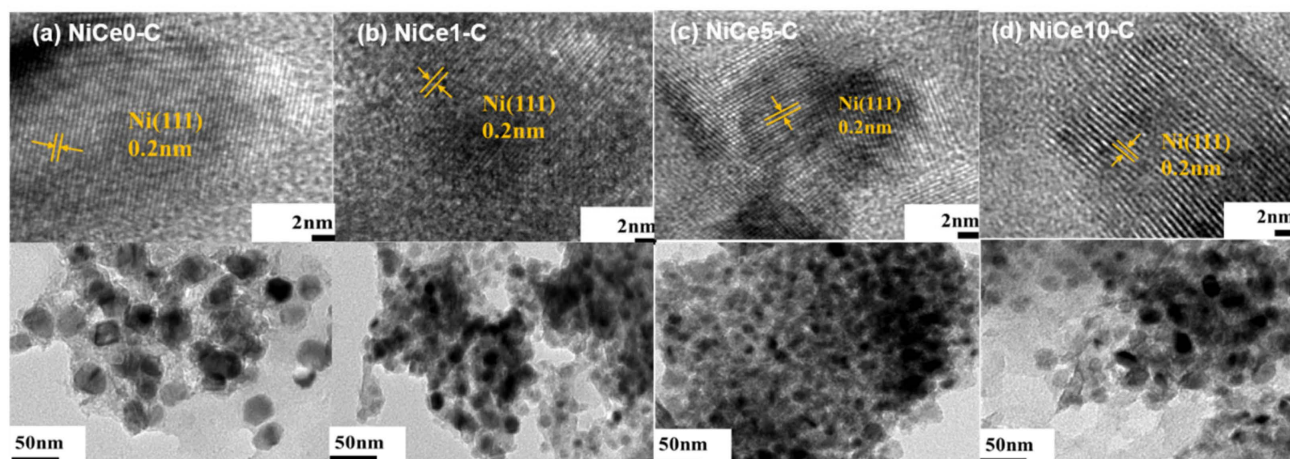


Figure 4. TEM and HRTEM images of the catalysts (a) NiCe0-C, (b) NiCe1-C, (c) NiCe5-C, and (d) NiCe10-C.

The particle-size frequency distribution and the average particle size were obtained by calculating the particle size of about 100 particles in the TEM image and plotting the frequency distribution histogram. As displayed in Figure 5, average particle size is in the range of 5–10 nm. The small size of the Ni nanoparticles is probably due to the confinement effect of the HT precursor [47], which processed that the ordered metal oxides grids would confine the growth of the Ni particles and achieve the highly dispersed Ni particles [48,49]. Meanwhile, the corresponding average particle size was found to follow the order: NiCe5-C (5.67 nm) < NiCe1-C (6.82 nm) < NiCe10-C (7.71 nm) < NiCe0-C (9.06 nm). Optimal Ce element loading (5 wt.%) led to the lowest Ni particle size. In a word, the statistics and TEM images proved that the aggregation of Ni particles in the NiCe0-C catalyst could be halted to some extent by the incorporation of the Ce element, which would play a positive effect on the uniform dispersion of the Ni nanoparticles.

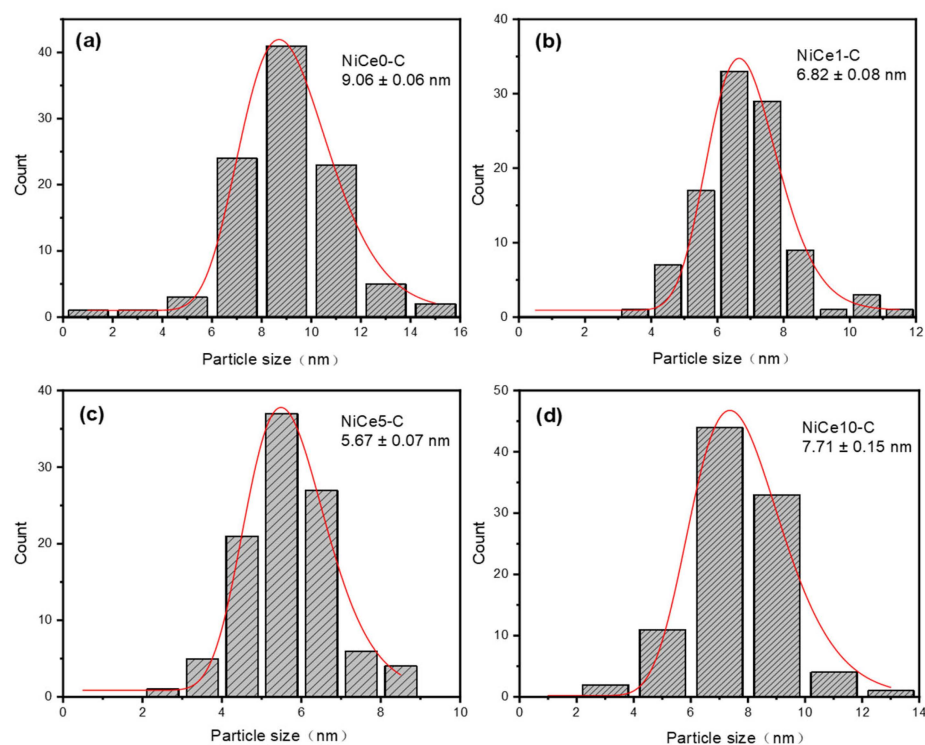


Figure 5. Metal particle size distribution over the reduced catalysts by TEM images, (a) NiCe0-C, (b) NiCe1-C, (c) NiCe5-C, and (d) NiCe10-C.

3.3. Reducibility and Metal-Support Interaction Study

The reduction behavior of the NiCe x -C ($x = 0, 1, 5, 10$) catalysts was evaluated by H₂-TPR analysis. H₂ consumption during the H₂-TPR experiments should be caused mainly by the reduction of the NiO species. It was known that the reduction difficulty of the NiO species might be determined by the metal-support interaction with the oxide support or the dispersion conditions over the support surface [41]. As shown in Figure 6, three types of reduction peaks could be observed. The low-temperature reduction peak (340~360 °C) of the NiO species can be ascribed to the weakly interacting Ni species with the support [50]. It could be found that the peak intensity (340~360 °C) gradually became weaker with the increasing of Ce contents. The peak temperature decreased to 346 °C over the NiCe1-C catalyst, compared to 360 °C for undoped NiCe0-C. These results indicated that after the addition of the Ce element, this part of NiO was more easily reducible [51]. The minor shoulder peak (~510 °C) was attributed to the reduction of a small amount of Ni²⁺ species, which are weakly bound to oxygen atoms at the Ni-O-Al (or Ce) interface, commonly reported in Ni/AlCeO- x catalysts [32]. Besides, for Ce-containing catalysts, this reduction peak also corresponded to the reduction of Ce⁴⁺ to Ce³⁺ species [52]. The main reduction peak appeared at 700 °C for the NiCe x -C catalysts, which was attributed to a stronger metal-support interaction between the NiO species and the support matrix (Mg(Ce)AlO) [26]. To obtain highly reduced samples, the reduction temperature in the activity test was chosen to be about 700 °C. The reduction temperature of NiO in the NiCe5-C catalyst especially shifted to the lowest temperature of 690 °C. Consequently, for these NiO species, the NiCe5-C catalyst displayed the best reduction behavior. However, when the Ce element was incorporated into the catalyst, the high temperature peak (~700 °C) became broader with lower intensity. This result indicated that the strong metal-support interaction was weakened by the loading of the Ce element [53]. Appropriate metal-support interactions would lead to more Ni⁰ active sites [54], thus giving preferable low-temperature catalytic activity.

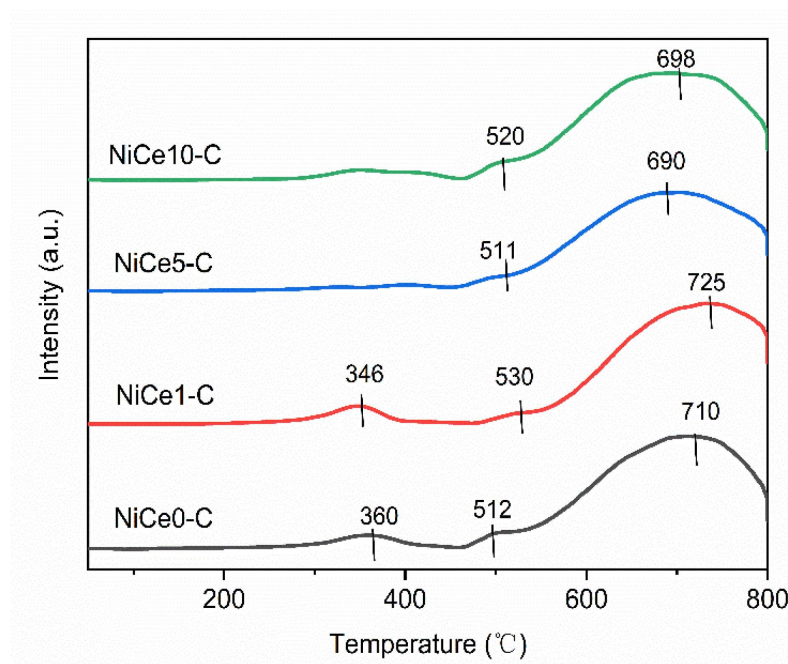


Figure 6. H₂-TPR profiles of NiCex-C (x = 0, 1, 5, 10) catalysts.

3.4. Surface Basicity and Element Distribution Analysis

In the CO₂ methanation process, the reaction molecule CO₂ was not directly absorbed on metal nickel, but on surface basic sites (OH[−] groups or alkali/alkaline-earth metal oxides), which was beneficial to activate CO₂ [21,55,56]. Hence, CO₂-TPD was carried out for the NiCex-C catalysts to determine the basic strength and CO₂ adsorption capacity. As shown in Figure 7, the desorption curves of all the samples could be divided into three types of Gaussian peaks (α , β , γ peaks). The three reduction peaks occurred at 100–120, 140–170, and 250–280 °C, respectively [7,11], which correspond to weak-strength basic sites (α and β peaks) and medium-strength basic sites (γ peak). The weak-strength basic sites were attributed to the rapid formation of bicarbonate, which was due to the weak adsorption of CO₂ by the hydroxyl group on the catalyst surface [14], while the medium basic sites were assigned to Lewis basic sites (acid-base Ce⁴⁺-O^{2−} and metal-O^{2−} pairs) associated with CO₂ adsorption. These basic sites bound CO₂ sufficiently strong for its activation and subsequent reduction [57]. Based on the literature [58], the medium basic sites played an important role in the CO₂ methanation process. From the previous report, the surface charge would be disturbed by introducing hetero-ions into the hydrotalcite layer [59]. Thus, the incorporation of the Ce element into the nickel-based hydrotalcite obviously influenced the distribution of basic sites. Detailed information of the surface basic sites' relative content for all reduced NiCex-C samples was displayed in Table 2. The proportion of the medium basic sites were calculated and were found to follow the order: NiCe5-C > NiCe1-C > NiCe0-C > NiCe10-C. The quantities of CO₂ adsorbed on basic sites over reduced NiCex-C catalysts were summarized in Table 3. The highest density of medium-strength basic sites was found on the NiCe5-C sample (0.79 mmol CO₂/g_{cat}), suggesting that CO₂ could be more easily activated and further affect the catalytic performance. The incorporation of 10 wt.% of the Ce element could lead to a slight decrease in total basicity (0.80 mmol CO₂/g_{cat}). The NiCe10-C exhibited the lowest CO₂ adsorption capacity, and thus, the least amount of CO₂ for the methanation. The correlation between the surface basic sites and its catalytic activity in the CO₂ methanation will be further explored in subsequent sections [60].

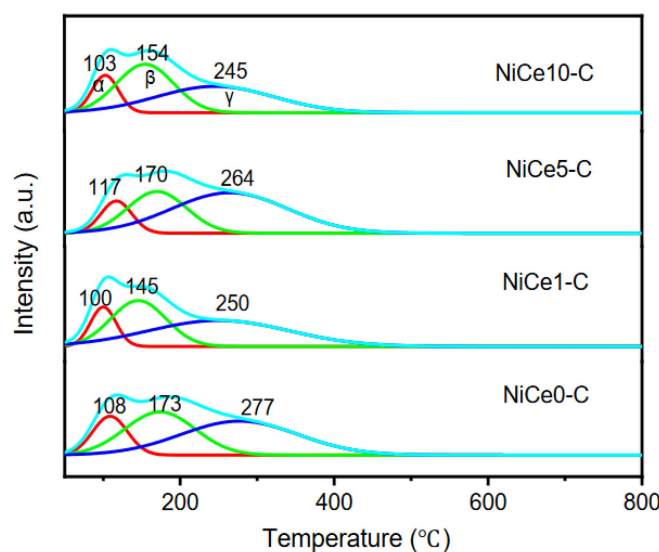


Figure 7. CO₂-TPD profiles of the NiCex-C catalysts; the red line indicated the α pick, the green line indicates the β -peak and the blue line indicates the γ -peak.

Table 2. Fitting analysis and parameters of CO₂-TPD for all reduced NiCex-C samples.

Samples	Reduction Temperature (°C)			Relative Content (%)		
	α	β	γ	α	β	γ
NiCe0-C	108	173	277	16.1	36.2	47.7
NiCe1-C	100	145	250	13.9	35.5	50.6
NiCe5-C	117	170	264	11.9	30.3	57.8
NiCe10-C	103	154	245	14.3	40.5	45.2

Table 3. Surface basic sites' density results of CO₂-TPD for all reduced NiCex-C samples.

Samples	Weak-Strength Basic Sites ($\alpha + \beta$) (mmol CO ₂ /g _{cat})	Medium-Strength Basic Sites (γ) (mmol CO ₂ /g _{cat})	CO ₂ -Adsorption Amount (mmol CO ₂ /g _{cat})
NiCe0-C	0.48	0.43	0.91
NiCe1-C	0.59	0.61	1.20
NiCe5-C	0.58	0.79	1.37
NiCe10-C	0.44	0.36	0.80

The information of the surface components for the NiCex-C catalysts was further probed by XPS measurements. It was known that the position of the most intense peak was used to confirm the oxidation state of the metallic element and to obtain the information about the charge density for its cations [31]. As displayed in Figure 8a, the main band of the Ni 2p_{3/2} spectra for all the NiCex-C catalysts were deconvoluted into three peaks at ~853.8, ~856.6, and ~862.3 eV, corresponding to Ni⁰, Ni²⁺ (bulk NiO), and satellite peak of nickel species [44]. From the literature, the satellite peak was assigned to Ni²⁺ species in the Ni-O-Ce interaction interface or Ni²⁺ species in unreducible NiAl₂O₄ spinel [61]. These Ni species at higher binding energy (~856 and ~862 eV) suggested the strong metal-support interaction [62]. Based on the peak fitting and peak area calculation, the detailed information of Ni⁰ species' relative contents were listed in Table 4. Compared with the Ce-free sample, the Ni⁰ relative content increased. In particular, the maximum value was 40.5% for the NiCe5-C catalyst, while the minimum value was 31.5% for the NiCe0-C catalyst. It was shown that the strong interaction between Ni²⁺ and support was weakened by the Ce dopants, leading to more Ni⁰ species generated, which was consistent with the

H₂-TPR results. Rare earth oxides might act as an electron donor so that more electrons were shifted to the Ni species, resulting in an increase of d-electron density on the Ni surface, similar to the reported (Sc, Y, Ce, and Pr) promoted NiMgAl catalysts for dry reforming of methane [63]. Meanwhile, this result also indicated that the introduction of Ce to the catalysts could promote the electron transfer and reduce more Ni²⁺ to Ni⁰. While the incorporation of Ce contents was further increased (10%), the proportion of Ni⁰ shifted to the lower value (34.1%).

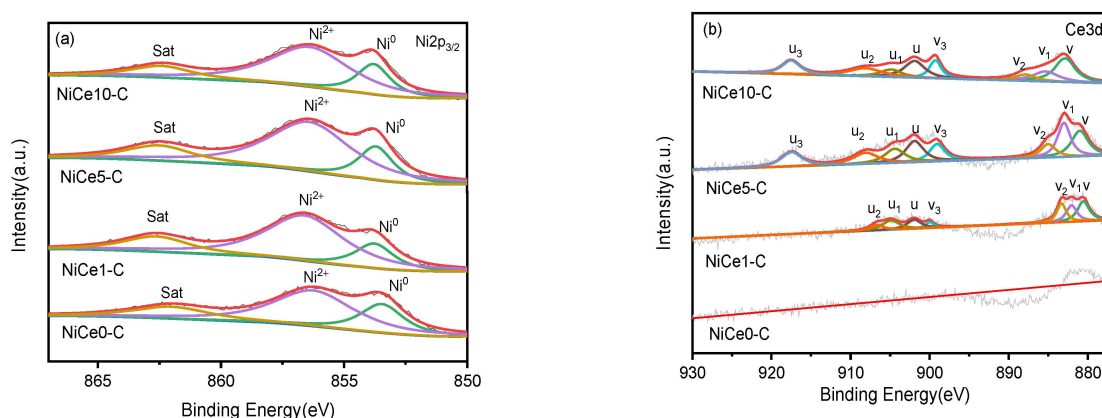


Figure 8. XPS spectrum of Ni 2p_{3/2} (a) and Ce3d (b) of the NiCex-C catalysts. In (a) the green line indicates the Ni⁰ species, the purple line indicates the Ni²⁺ species, the brown line indicates satellite peaks, and the red line is the original curve.

Table 4. XPS result of Ni⁰ and Ce³⁺ relative content for the NiCex-C catalysts.

Samples	Relative Content (%)	
	Ni ⁰ /(Ni ⁰ + Ni ²⁺)	Ce ³⁺ /(Ce ³⁺ + Ce ⁴⁺)
NiCe0-C	31.5	0.0
NiCe1-C	34.7	19.6
NiCe5-C	40.5	23.2
NiCe10-C	34.1	18.8

On the other hand, the two sets of Ce 3d spin–orbit coupling peaks, corresponding to 3d_{3/2} (labeled as u) and 3d_{5/2} (labeled as v), respectively, could be deconvoluted into eight peaks (Figure 8b). According to the literature, the oxidation states of cerium species mainly existed in the form of Ce³⁺ and Ce⁴⁺ [1]. More precisely, the peaks near 882.8 eV (v), 887.8 eV (v₂), 899.2 eV (v₃), 901.9 eV (u), 908.1 eV (u₂), and 917.5 eV (u₃) could be attributed to the Ce⁴⁺ species in CeO₂ [50]. However, for the NiCe1-C catalyst with lower Ce-loading, the u₃ peak near 917.5 eV was not noticeable from XPS spectra. Additionally, the peak near 885.3 eV (v₁) 904.9 eV (u₁) could be ascribed to the Ce³⁺ state [64]. The Ce³⁺ state indicated the reduction of Ce⁴⁺ due to the high-temperature hydrogen reduction [45]. In order to keep charge balance of CeO₂, oxygen vacancies were generated in this reduction process [50,65]. Thus, the concentration of Ce³⁺ was in direct proportion to oxygen vacancy contents, which were the main active sites in CO₂ activation and absorption [8,66]. The concentrations of Ce³⁺ of all the NiCex-C catalysts were calculated by adding the areas under each deconvolution peak and dividing by the total peak area. The detailed molar ratio of Ce³⁺/(Ce³⁺ + Ce⁴⁺) was tabulated in Table 4. It could be found the highest Ce³⁺ concentration of 23.2% for the NiCe5-C catalyst was obviously higher than other Ce-containing catalysts, demonstrating that there were more oxygen vacancies at the Ni–O–Ce interfaces. In a word, the NiCe5-C catalyst owned the most active sites for CO₂ absorption and activation, as well as surface Ni⁰ sites for the H₂ molecular splitting. They may work synergistically and efficiently in CO₂ hydrogenation under this reaction condition.

3.5. Catalytic Activity and Stability in CO₂ Methanation Reaction

The catalytic performance of all prepared NiCe_x-C ($x = 0, 1, 5, 10$) catalysts for the CO₂ methanation reaction were investigated at gas hourly space velocity (GHSV) of inlet gas of 15,000 mL/g_{cat}/h with an H₂/CO₂ molar ratio of 4.0 in the temperature range of 200–350 °C. It was known that the CO₂ methanation process was exothermic, so the total conversion could not be reached to 100% at high reaction temperature (>200 °C) [37]. CO₂ methanation performances of the NiCe_x-C catalysts were shown in Figure 9. As shown in Figure 9a, CO₂ conversion increased for all the samples with increasing reaction temperature. A significant difference in performance was displayed at 250 °C. CO₂ conversion increased at 250 °C from 11.7% for NiCe0-C to 30.2% and 80.0% for NiCe1-C and NiCe5-C, respectively. The maximum CO₂ conversion was observed at 300 °C. Then the catalysts reached CO₂ equilibrium conversion above 300 °C. T₅₀ was used to identify the low-temperature activity of the samples [11]. The value of T₅₀ was 263.8 °C and 258.4 °C for the Ce-free NiCe0-C catalyst and the NiCe1-C catalyst, respectively, while it was obviously decreased to 238.6 °C for the NiCe5-C catalyst, indicating the promotion effect from Ce. However, when further increasing Ce content, the value of T₅₀ increased to 277.9 °C for the NiCe10-C catalyst. It could be found that the catalytic performance first increased and then decreased with the increase of Ce content. This excellent low-temperature performance of NiCe5-C was from two main aspects: (I) Abundant active Ni⁰ sites evenly dispersed over the NiMgAl mixed metal oxide surface (XPS and TEM results), which provided active metal sites for H₂ molecular dissociation and further promoted the hydrogenation process [41]. (II) The medium basic sites were conducive to the CO₂ adsorption and activation [20]. NiCe5-C possessed the highest amounts of medium-strength basic sites (CO₂-TPD result). Nevertheless, NiCe10-C exhibited the worst hydrogenation activity. This could have been mainly caused by the lowest amounts of total basic sites, as confirmed by CO₂-TPD. Furthermore, CO as the main byproduct in the CO₂ methanation process was due to the reverse water gas shift (RWGS) process: CO₂ + H₂ = CO + H₂O. It is an endothermic reaction favorable at high temperature [67]. The CH₄ selectivity of NiCe_x-C catalysts presented a high value of nearly 100% (Figure 9b), and few CO byproducts could be found at low reaction temperatures. The detailed product distributions of the tested catalysts in the CO₂ methanation reaction at a reaction temperature of 225 °C were displayed in Table 5. At 225 °C, the CO₂ conversion of the Ce-free sample was only 3.4%, while that of NiCe5-C reached a maximum value of 13.9%. The CO₂ conversion rate (R_{CO_2}) and the TOF (turnover frequency) values of NiCe5-C were 4.1 times and 3 times higher than that of NiCe0-C, respectively. It indicated that the low-temperature activity of the Ni-based catalysts derived from hydrotalcite-like precursors could be significantly enhanced by moderate Ce doping. The activity of Ni-based catalysts for low-temperature CO₂ methanation reported in the literature over the last decade was also compared, as shown in Table 6. The CO₂ conversion of the NiCe5-C catalyst in this work is better than those reported in other literature [13,34,68–73] at a low temperature of 250 °C.

The long-term stability of the catalyst was of great importance for industrial application. Catalysts are prone to sintering under high-temperature conditions, which can lead to catalyst deactivation [3]. Therefore, the stability of the catalyst was judged by testing the CO₂ conversion and CH₄ selectivity at higher reaction temperatures (300 °C) and whether there were significant changes under prolonged operation as indicators. After 80 h of the stability test, as shown in Figure 10, the NiCe5-C catalyst also exhibited high activity, with about 91.7% of CO₂ conversion and almost 100% of CH₄ selectivity. In addition, there was no obvious deviation for them under the 80-h stability test. It indicated that the well-dispersed nickel particles on the catalyst surface (TEM results) could enhance the anti-sintering ability of the NiCe5-C sample and avoid deactivation after long-term use. The XRD spectra of the NiCe5-C catalyst after the 80-h stability test was shown in Figure 11. The crystalline phase remained essentially the same compared with that of the fresh NiCe5-C catalyst, which proves the stability of the catalyst structure after this reaction.

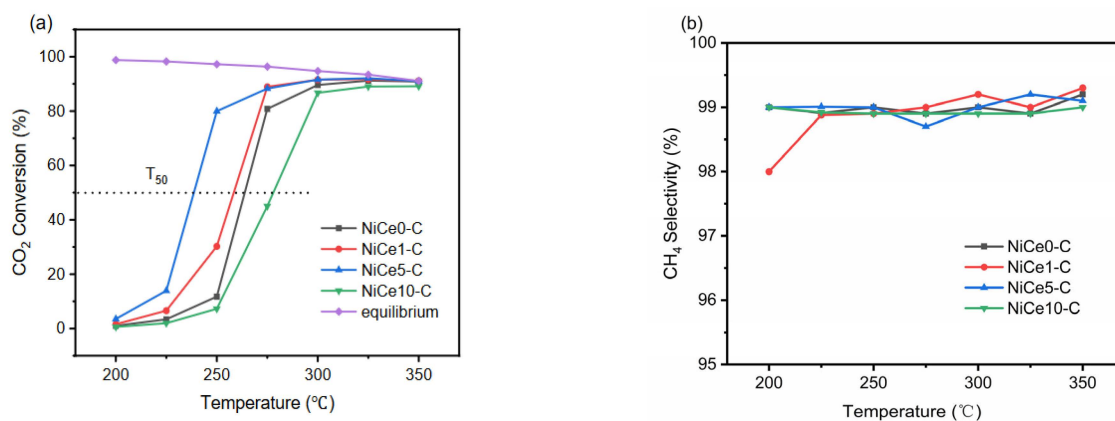


Figure 9. CO₂ conversion (a,b) CH₄ selectivity of NiCex-C catalysts with a temperature range from 200 to 350 °C, GHSV = 15,000 mL/g_{cat}/h H₂/CO₂ = 4 (molar ratio), 50 mL/min, 200 mg catalyst.

Table 5. Comparison of the catalytic performance of NiCex-C (x = 0, 1, 5, 10) catalysts in CO₂ methanation at 225 °C.

Samples	Conversion (%)	Selectivity (%)		R _{CO₂} (μmolCO ₂ /g _{cat} /s)	TOF (h ⁻¹)
		CH ₄	CO		
NiCe0-C	3.4	98.7	1.3	1.26	3.9
NiCe1-C	6.6	98.9	1.1	2.43	6.6
NiCe5-C	13.9	99.0	1.0	5.17	11.9
NiCe10-C	2.0	98.9	1.1	0.73	2.2

Reaction conditions: T = 225 °C (conversion < 15%), GHSV = 15,000 mL/g_{cat}/h, H₂/CO₂ = 4 (molar ratio), 50 mL/min, 200 mg catalyst.

Table 6. Comparison of catalyst activity for CO₂ methanation reactions in the last decade.

Catalyst	Temperature (°C)	The Inert Gas Ratio of H ₂ /CO ₂	CO ₂ Conversion (%)	CH ₄ Selectivity (%)	Reference
NiCe5-C	250	H ₂ :CO ₂ = 4	80.0	99.0	This work
Ni20Fe1.5	250	H ₂ :CO ₂ = 4	71.0	99.0	[68]
HTNi15Cu1	250	H ₂ :CO ₂ = 4	9.0	89.0	[69]
Ni21La0.4	250	H ₂ :CO ₂ = 4	55.0	99.0	[70]
Ni42.5	250	H ₂ :CO ₂ = 4	72.0	99.9	[34]
Ni/CeO ₂	250	H ₂ :CO ₂ = 4	30.0	99.9	[71]
Ni-La/SiC	250	H ₂ :CO ₂ = 4	39.6	99.6	[72]
12Ni6Ce/CNT	250	H ₂ :CO ₂ = 4	32.0	99.9	[73]
NiW1MgOX	250	H ₂ :CO ₂ = 4	38.0	99.9	[13]

Hydrogenation of CO₂ to methane was a first order reaction, and the reaction of H with CO₂ was the rate-controlling step for this reaction [74]. The apparent activation energies of the samples were measured by the Arrhenius equation. As shown in Figure 12, the logarithm of CO₂ conversion as x variable and the reciprocal of temperature as y variable fit a straight line. The apparent activation energies of the catalysts were obtained by calculating the slope of the fitting lines. Compared to the NiCe0-C catalyst (98.13 kJ/mol), the apparent activation energy of the NiCe5-C catalyst was lower (96.04 kJ/mol). This result suggested that the CO₂ methanation reaction was more facile on the NiCe5-C catalyst. It was contributed to the remarkable promotion effect of cerium on promoting charge transfer from active metal to the CO₂ molecules [73]. Therefore, the reactant CO₂ molecules were more easily activated, which is in favor of decreasing the energy barrier of the H and CO₂ reaction.

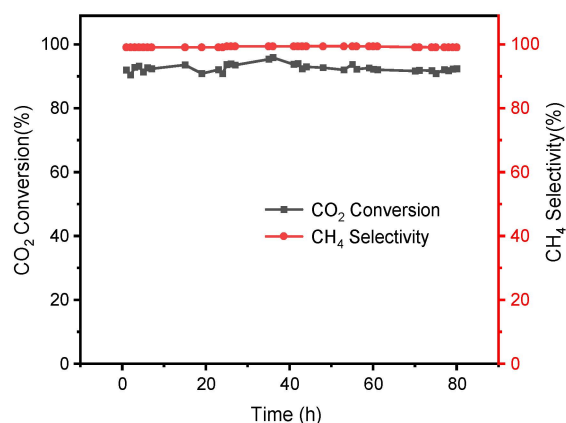


Figure 10. Stability for CO₂ methanation over the NiCe5-C catalyst at 300 °C. Reaction conditions: H₂/CO₂ = 4:1, GHSV = 15,000 mL/g_{cat}/h, 0.1Mpa.

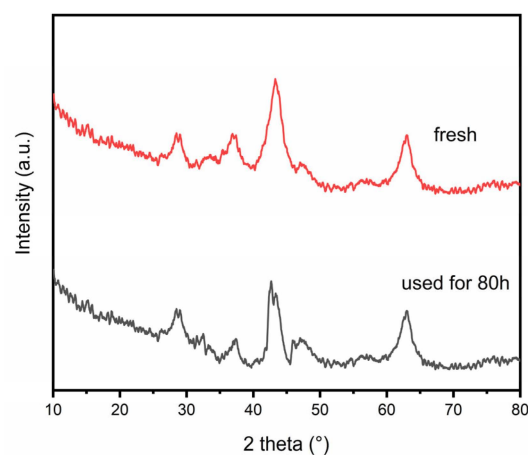


Figure 11. Comparison of XRD patterns of the NiCe5-C catalyst before and after the 80-h stability test.

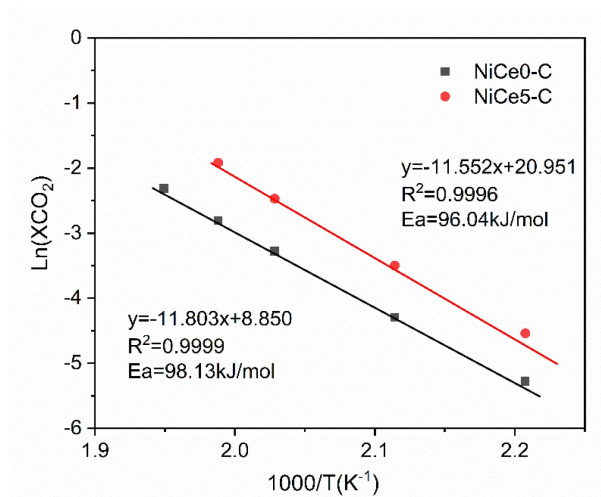


Figure 12. Arrhenius plots for the NiCe0-C and NiCe5-C catalysts.

3.6. The Descriptors of the Relationship between Catalytic Performance and Surface Basicity

On the basis of previous literature reports, the Lewis acid-base sites instead of strong basic sites were involved in the CO₂ methanation mechanism [75,76]. Therefore, it was necessary to explore the relationship between catalytic activity and the number of medium basic sites. As plotted in Figure 13a, the highest CO₂ conversion at 225 °C was achieved

over the NiCe5-C with the strongest medium-strength basic sites. In addition, the CO₂ conversion of the catalysts was positively correlated with the number of medium basic sites. In this contribution, we observed the turnover frequency of the catalysts almost displayed linear relationship with the content of medium-strength basic sites at 225 °C (Figure 13b). It showed that the TOF values increased with increasing amounts of medium-strength basic sites. These results demonstrate that the variation of Ce content could effectively regulate the number of medium-strength basic sites on the surface of NiCex-C, and the medium-strength basic sites on the catalyst played a crucial role in achieving high catalytic activity for CO₂ methanation at low temperatures.

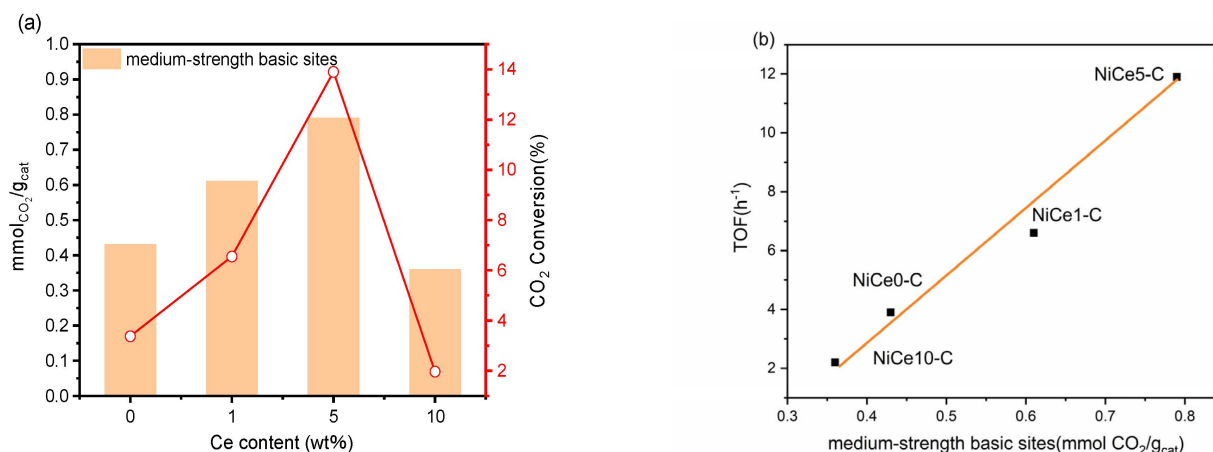


Figure 13. (a) Effect of Ce content on the medium-strength basic sites and CO₂ conversion (T = 225 °C). (b) The relationship between medium-strength basic sites and TOF (T = 225 °C).

4. Conclusions

In this work, we demonstrated an extremely straightforward method of preparing Ce-promoted NiMgAl hydrotalcite-derived catalysts via a co-precipitation operation to promote CO₂ methanation at low temperatures. The NiCe5-C sample exhibited superior low-temperature activity for CO₂ methanation (CO₂ conversion: 80.0%, CH₄ selectivity >99%, GHSV = 15,000 mL/gcat/h, H₂/CO₂ = 4, 250 °C, 0.1 Mpa), together with high stability, while the CO₂ conversion of the Ce-free sample was only 11.7% under the same conditions. At 225 °C, the TOF value of NiCe5-C (11.9 h⁻¹) was three times higher than that of NiCe0-C (3.9 h⁻¹). The characterization results indicated that the incorporation of the appropriate amount of Ce into NiMgAl could weaken the strong metal-support interaction, thereby promoting the reduction of the NiO species. Meanwhile, the Ce element could efficiently regulate the surface basic species. The medium-basic sites were found to have a good linear correlation with TOF. The NiCe5-C catalyst with the highest Ni⁰/(Ni²⁺ + Ni⁰) ratio and abundant medium-basic sites was found to be exceptionally effective at dissociating H₂ and activating CO₂. In addition, it was able to hydrogenate methane with great efficiency. Our contribution provided a promising and practical thought to raise the catalytic performance in CO₂ methanation at low temperature.

Author Contributions: Conceptualization, Y.P. and X.X.; methodology, Y.P.; software, Y.P. validation, X.X. and W.C.; formal analysis, Y.P.; investigation, Y.P. and X.X.; resources, X.X. and W.C.; data curation, Y.P.; writing—original draft preparation, Y.P.; writing—review and editing, Y.P., X.X., L.S., N.W. and W.C.; visualization, Y.P. and X.X.; supervision, X.X., W.C. and N.W.; project administration, X.X. and W.C.; funding acquisition, X.X. All authors have read and agreed to the published version of the manuscript.

Funding: This research was funded by Sichuan Science and Technology Program (2023YFS0354).

Institutional Review Board Statement: Not applicable.

Informed Consent Statement: Not applicable.

Data Availability Statement: No new data created.

Conflicts of Interest: The authors declare no conflict of interest.

References

1. Bian, Y.; Xu, C.; Wen, X.; Xu, L.; Cui, Y.; Wang, S.; Wu, C.-E.; Qiu, J.; Cheng, G.; Chen, M. CO₂ methanation over the Ni-based catalysts supported on nano-CeO₂ with varied morphologies. *Fuel* **2023**, *331*, 125755. [[CrossRef](#)]
2. Tada, S.; Kikuchi, R. Mechanistic study and catalyst development for selective carbon monoxide methanation. *Catal. Sci. Technol.* **2015**, *5*, 3061–3070. [[CrossRef](#)]
3. Lin, J.; Ma, C.; Wang, Q.; Xu, Y.; Ma, G.; Wang, J.; Wang, H.; Dong, C.; Zhang, C.; Ding, M. Enhanced low-temperature performance of CO₂ methanation over mesoporous Ni/Al₂O₃-ZrO₂ catalysts. *Appl. Catal. B Environ.* **2019**, *243*, 262–272.
4. Varvoutis, G.; Lykaki, M.; Stefa, S.; Binas, V.; Marnellos, G.E.; Konsolakis, M. Deciphering the role of Ni particle size and nickel-ceria interfacial perimeter in the low-temperature CO₂ methanation reaction over remarkably active Ni/CeO₂ nanorods. *Appl. Catal. B Environ.* **2021**, *297*, 120401. [[CrossRef](#)]
5. Kopyscinski, J.; Schildhauer, T.J.; Biollaz, S.M.A. Production of synthetic natural gas (SNG) from coal and dry biomass—A technology review from 1950 to 2009. *Fuel* **2010**, *89*, 1763–1783. [[CrossRef](#)]
6. Zhen, W.; Gao, F.; Tian, B.; Ding, P.; Deng, Y.; Li, Z.; Gao, H.; Lu, G. Enhancing activity for carbon dioxide methanation by encapsulating (1 1 1) facet Ni particle in metal–organic frameworks at low temperature. *J. Catal.* **2017**, *348*, 200–211.
7. Summa, P.; Swirk, K.; Wierzbicki, D.; Motak, M.; Alxneit, I.; Ronning, M.; Da Costa, P. Co-Precipitated Ni-Mg-Al Hydrotalcite-Derived Catalyst Promoted with Vanadium for CO₂ Methanation. *Molecules* **2021**, *26*, 6506. [[CrossRef](#)]
8. Rui, N.; Zhang, X.; Zhang, F.; Liu, Z.; Cao, X.; Xie, Z.; Zou, R.; Senanayake, S.D.; Yang, Y.; Rodriguez, J.A.; et al. Highly active Ni/CeO₂ catalyst for CO₂ methanation: Preparation and characterization. *Appl. Catal. B Environ.* **2021**, *282*, 119581. [[CrossRef](#)]
9. Aziz, M.A.A.; Jalil, A.A.; Triwahyono, S.; Ahmad, A. CO₂ methanation over heterogeneous catalysts: Recent progress and future prospects. *Green Chem.* **2015**, *17*, 2647–2663. [[CrossRef](#)]
10. Mutz, B.; Carvalho, H.W.P.; Mangold, S.; Kleist, W.; Grunwaldt, J.-D. Methanation of CO₂: Structural response of a Ni-based catalyst under fluctuating reaction conditions unraveled by operando spectroscopy. *J. Catal.* **2015**, *327*, 48–53. [[CrossRef](#)]
11. Xiao, X.; Wang, J.; Li, J.; Dai, H.; Jing, F.; Liu, Y.; Chu, W. Enhanced low-temperature catalytic performance in CO₂ hydrogenation over Mn-promoted NiMgAl catalysts derived from quaternary hydrotalcite-like compounds. *Int. J. Hydrogen Energy* **2021**, *46*, 33107–33119. [[CrossRef](#)]
12. Ma, L.; Ye, R.; Huang, Y.; Reina, T.R.; Wang, X.; Li, C.; Zhang, X.L.; Fan, M.; Zhang, R.; Liu, J. Enhanced low-temperature CO₂ methanation performance of Ni/ZrO₂ catalysts via a phase engineering strategy. *Chem. Eng. J.* **2022**, *446*, 137031. [[CrossRef](#)]
13. Yan, Y.; Dai, Y.; He, H.; Yu, Y.; Yang, Y. A novel W-doped Ni-Mg mixed oxide catalyst for CO₂ methanation. *Appl. Catal. B Environ.* **2016**, *196*, 108–116. [[CrossRef](#)]
14. He, F.; Zhuang, J.; Lu, B.; Liu, X.; Zhang, J.; Gu, F.; Zhu, M.; Xu, J.; Zhong, Z.; Xu, G.; et al. Ni-based catalysts derived from Ni-Zr-Al ternary hydrotalcites show outstanding catalytic properties for low-temperature CO₂ methanation. *Appl. Catal. B Environ.* **2021**, *293*, 120218. [[CrossRef](#)]
15. Liu, H.; Min, E. Catalytic oxidation of mercaptans by bifunctional catalysts composed of cobalt phthalocyanine supported on Mg–Al hydrotalcite-derived solid bases: Effects of basicity. *Green Chem.* **2006**, *8*, 657–662. [[CrossRef](#)]
16. He, L.; Lin, Q.; Liu, Y.; Huang, Y. Unique catalysis of Ni-Al hydrotalcite derived catalyst in CO₂ methanation: Cooperative effect between Ni nanoparticles and a basic support. *J. Energy Chem.* **2014**, *23*, 587–592. [[CrossRef](#)]
17. Dębek, R.; Radlik, M.; Motak, M.; Galvez, M.E.; Turek, W.; Da Costa, P.; Grzybek, T. Ni-containing Ce-promoted hydrotalcite derived materials as catalysts for methane reforming with carbon dioxide at low temperature—On the effect of basicity. *Catal. Today* **2015**, *257*, 59–65. [[CrossRef](#)]
18. Li, C.; Wei, M.; Evans, D.G.; Duan, X. Layered double hydroxide-based nanomaterials as highly efficient catalysts and adsorbents. *Small* **2014**, *10*, 4469–4486. [[CrossRef](#)]
19. Liu, J.; Bing, W.; Xue, X.; Wang, F.; Wang, B.; He, S.; Zhang, Y.; Wei, M. Alkaline-assisted Ni nanocatalysts with largely enhanced low-temperature activity toward CO₂ methanation. *Catal. Sci. Technol.* **2016**, *6*, 3976–3983. [[CrossRef](#)]
20. Guo, X.; Gao, D.; He, H.; Traitangwong, A.; Gong, M.; Meeyoo, V.; Peng, Z.; Li, C. Promotion of CO₂ methanation at low temperature over hydrotalcite-derived catalysts-effect of the tunable metal species and basicity. *Int. J. Hydrogen Energy* **2021**, *46*, 518–530. [[CrossRef](#)]
21. Wang, J.; Xiao, X.; Li, J.; Gao, X.; Zheng, J.; Chu, W. Hydrotalcite-derived Ni-LDO catalysts via new approach for enhanced performances in CO₂ catalytic reduction. *Fuel* **2022**, *324*, 124491. [[CrossRef](#)]
22. Wang, Y.; Xu, Y.; Liu, Q.; Sun, J.; Ji, S.; Wang, Z.J. Enhanced low-temperature activity for CO₂ methanation over NiMgAl₂SiC. *J. Chem. Technol. Biotechnol.* **2019**, *94*, 3780–3786. [[CrossRef](#)]
23. Du, X.; Zhang, D.; Gao, R.; Huang, L.; Shi, L.; Zhang, J. Design of modular catalysts derived from NiMgAl-LDH@m-SiO₂ with dual confinement effects for dry reforming of methane. *Chem. Commun.* **2013**, *49*, 6770–6772. [[CrossRef](#)] [[PubMed](#)]
24. Sun, C.; Świrk, K.; Wierzbicki, D.; Motak, M.; Grzybek, T.; Da Costa, P. On the effect of yttrium promotion on Ni-layered double hydroxides-derived catalysts for hydrogenation of CO₂ to methane. *Int. J. Hydrogen Energy* **2021**, *46*, 12169–12179. [[CrossRef](#)]

25. Wierzbicki, D.; Debek, R.; Motak, M.; Grzybek, T.; Gálvez, M.E.; Da Costa, P. Novel Ni-La-hydroxalcalite derived catalysts for CO₂ methanation. *Catal. Commun.* **2016**, *83*, 5–8. [[CrossRef](#)]
26. Taufiq-Yap, Y.H.; Sudarno; Rashid, U.; Zainal, Z. CeO₂-SiO₂ supported nickel catalysts for dry reforming of methane toward syngas production. *Appl. Catal. A Gen.* **2013**, *468*, 359–369. [[CrossRef](#)]
27. Montini, T.; Melchionna, M.; Monai, M.; Fornasiero, P. Fundamentals and Catalytic Applications of CeO₂-Based Materials. *Chem. Rev.* **2016**, *116*, 5987–6041. [[CrossRef](#)]
28. Wu, L.; Xie, X.; Ren, H.; Gao, X. A short review on nickel-based catalysts in dry reforming of methane: Influences of oxygen defects on anti-coking property. *Mater. Today Proc.* **2021**, *42*, 153–160. [[CrossRef](#)]
29. Vasiliades, M.A.; Damaskinos, C.M.; Djinić, P.; Pintar, A.; Efstathiou, A.M. A transient isotopic study for investigating important design parameters of NiCo/Ce_{0.75}Zr_{0.25}O_{2-δ} catalyst for the dry reforming of methane. *Catal. Commun.* **2023**, *178*, 106674. [[CrossRef](#)]
30. Debek, R.; Motak, M.; Galvez, M.E.; Grzybek, T.; Da Costa, P. Influence of Ce/Zr molar ratio on catalytic performance of hydroxalcalite-derived catalysts at low temperature CO₂ methane reforming. *Int. J. Hydrogen Energy* **2017**, *42*, 23556–23567. [[CrossRef](#)]
31. Cárdenas-Arenas, A.; Quindimil, A.; Davó-Quiñonero, A.; Bailón-García, E.; Lozano-Castelló, D.; De-La-Torre, U.; Pereda-Ayo, B.; González-Marcos, J.A.; González-Velasco, J.R.; Bueno-López, A. Isotopic and in situ DRIFTS study of the CO₂ methanation mechanism using Ni/CeO₂ and Ni/Al₂O₃ catalysts. *Appl. Catal. B Environ.* **2020**, *265*, 118538. [[CrossRef](#)]
32. Zhang, J.; Ren, B.; Fan, G.; Yang, L.; Li, F. Exceptional low-temperature activity of a perovskite-type AlCeO₃ solid solution-supported Ni-based nanocatalyst towards CO₂ methanation. *Catal. Sci. Technol.* **2021**, *11*, 3894–3904.
33. Debek, R.; Galvez, M.E.; Launay, F.; Motak, M.; Grzybek, T.; Da Costa, P. Low temperature dry methane reforming over Ce, Zr and CeZr promoted Ni-Mg-Al hydroxalcalite-derived catalysts. *Int. J. Hydrogen Energy* **2016**, *41*, 11616–11623. [[CrossRef](#)]
34. Wierzbicki, D.; Baran, R.; Debek, R.; Motak, M.; Grzybek, T.; Gálvez, M.E.; Da Costa, P. The influence of nickel content on the performance of hydroxalcalite-derived catalysts in CO₂ methanation reaction. *Int. J. Hydrogen Energy* **2017**, *42*, 23548–23555. [[CrossRef](#)]
35. Lin, S.; Hao, Z.; Shen, J.; Chang, X.; Huang, S.; Li, M.; Ma, X. Enhancing the CO₂ methanation activity of Ni/CeO₂ via activation treatment-determined metal-support interaction. *J. Energy Chem.* **2021**, *59*, 334–342. [[CrossRef](#)]
36. Guo, X.; Peng, Z.; Hu, M.; Zuo, C.; Traitangwong, A.; Meeyoo, V.; Li, C.; Zhang, S. Highly Active Ni-Based Catalyst Derived from Double Hydroxides Precursor for Low Temperature CO₂ Methanation. *Ind. Eng. Chem. Res.* **2018**, *57*, 9102–9111. [[CrossRef](#)]
37. Gao, J.; Jiang, Q.; Liu, Y.; Liu, W.; Chu, W.; Su, D.S. Probing the enhanced catalytic activity of carbon nanotube supported Ni-LaO_x hybrids for the CO₂ reduction reaction. *Nanoscale* **2018**, *10*, 14207–14219. [[CrossRef](#)]
38. Wang, X.; Liu, Q.; Jiang, J.; Jin, G.; Li, H.; Gu, F.; Xu, G.; Zhong, Z.; Su, F. SiO₂-stabilized Ni/t-ZrO₂ catalysts with ordered mesopores: One-pot synthesis and their superior catalytic performance in CO methanation. *Catal. Sci. Technol.* **2016**, *6*, 3529–3543. [[CrossRef](#)]
39. Xu, X.; Liu, L.; Tong, Y.; Fang, X.; Xu, J.; Jiang, D.-e.; Wang, X. Facile Cr³⁺-Doping Strategy Dramatically Promoting Ru/CeO₂ for Low-Temperature CO₂ Methanation: Unraveling the Roles of Surface Oxygen Vacancies and Hydroxyl Groups. *ACS Catal.* **2021**, *11*, 5762–5775. [[CrossRef](#)]
40. Asencios, Y.J.O.; Elias, K.F.M.; Assaf, E.M. Oxidative-reforming of model biogas over NiO/Al₂O₃ catalysts: The influence of the variation of support synthesis conditions. *Appl. Surf. Sci.* **2014**, *317*, 350–359. [[CrossRef](#)]
41. Zhang, Q.; Xu, R.; Liu, N.; Dai, C.; Yu, G.; Wang, N.; Chen, B. In situ Ce-doped catalyst derived from NiCeAl-LDHs with enhanced low-temperature performance for CO₂ methanation. *Appl. Surf. Sci.* **2022**, *579*, 152204. [[CrossRef](#)]
42. Tanasoi, S.; Mitran, G.; Tanchoux, N.; Cacciaguerra, T.; Fajula, F.; Săndulescu, I.; Tichit, D.; Marcu, I.-C. Transition metal-containing mixed oxides catalysts derived from LDH precursors for short-chain hydrocarbons oxidation. *Appl. Catal. A Gen.* **2011**, *395*, 78–86. [[CrossRef](#)]
43. Tao, M.; Meng, X.; Lv, Y.; Bian, Z.; Xin, Z. Effect of impregnation solvent on Ni dispersion and catalytic properties of Ni/SBA-15 for CO methanation reaction. *Fuel* **2016**, *165*, 289–297. [[CrossRef](#)]
44. Kim, M.-J.; Youn, J.-R.; Kim, H.J.; Seo, M.W.; Lee, D.; Go, K.S.; Lee, K.B.; Jeon, S.G. Effect of surface properties controlled by Ce addition on CO₂ methanation over Ni/Ce/Al₂O₃ catalyst. *Int. J. Hydrogen Energy* **2020**, *45*, 24595–24603. [[CrossRef](#)]
45. Guo, X.; He, H.; Traitangwong, A.; Gong, M.; Meeyoo, V.; Li, P.; Li, C.; Peng, Z.; Zhang, S. Ceria imparts superior low temperature activity to nickel catalysts for CO₂ methanation. *Catal. Sci. Technol.* **2019**, *9*, 5636–5650. [[CrossRef](#)]
46. Bette, N.; Thielemann, J.; Schreiner, M.; Mertens, F. Methanation of CO₂ over a (Mg,Al)O_x Supported Nickel Catalyst Derived from a (Ni,Mg,Al)-Hydroxalcalite-like Precursor. *ChemCatChem* **2016**, *8*, 2903–2906. [[CrossRef](#)]
47. Du, X.; Zhang, D.; Shi, L.; Gao, R.; Zhang, J. Coke- and sintering-resistant monolithic catalysts derived from in situ supported hydroxalcalite-like films on Al wires for dry reforming of methane. *Nanoscale* **2013**, *5*, 2659–2663. [[CrossRef](#)]
48. Xiao, X.; Gao, J.; Xi, S.; Lim, S.H.; Png, A.K.W.; Borgna, A.; Chu, W.; Liu, Y. Experimental and in situ DRIFTS studies on confined metallic copper stabilized Pd species for enhanced CO₂ reduction to formate. *Appl. Catal. B Environ.* **2022**, *309*, 121239. [[CrossRef](#)]
49. Duarte, R.B.; Nachttegaal, M.; Bueno, J.M.C.; van Bokhoven, J.A. Understanding the effect of Sm₂O₃ and CeO₂ promoters on the structure and activity of Rh/Al₂O₃ catalysts in methane steam reforming. *J. Catal.* **2012**, *296*, 86–98. [[CrossRef](#)]

50. Du, Y.; Qin, C.; Xu, Y.; Xu, D.; Bai, J.; Ma, G.; Ding, M. Ni nanoparticles dispersed on oxygen vacancies-rich CeO₂ nanoplates for enhanced low-temperature CO₂ methanation performance. *Chem. Eng. J.* **2021**, *418*, 129402. [[CrossRef](#)]
51. Sato, A.G.; Volanti, D.P.; Meira, D.M.; Damyanova, S.; Longo, E.; Bueno, J.M.C. Effect of the ZrO₂ phase on the structure and behavior of supported Cu catalysts for ethanol conversion. *J. Catal.* **2013**, *307*, 1–17. [[CrossRef](#)]
52. Amin, R.; Chang, X.; Liu, B. Synergistic Effect of CeO₂ in CH₄/CO₂ Dry Reforming Reaction over Stable $x\text{CeO}_2\text{-}y\text{Ni}/\text{MCM-22}$ Catalysts. *Ind. Eng. Chem. Res.* **2017**, *56*, 7445–7453. [[CrossRef](#)]
53. Wu, Y.; Lin, J.; Ma, G.; Xu, Y.; Zhang, J.; Samart, C.; Ding, M. Ni nanocatalysts supported on mesoporous Al₂O₃-CeO₂ for CO₂ methanation at low temperature. *RSC Adv.* **2020**, *10*, 2067–2072. [[CrossRef](#)]
54. Li, W.; Liu, Y.; Mu, M.; Ding, F.; Liu, Z.; Guo, X.; Song, C. Organic acid-assisted preparation of highly dispersed Co/ZrO₂ catalysts with superior activity for CO₂ methanation. *Appl. Catal. B Environ.* **2019**, *254*, 531–540. [[CrossRef](#)]
55. Saththawong, R.; Koizumi, N.; Song, C.; Prasassarakich, P. Bimetallic Fe–Co catalysts for CO₂ hydrogenation to higher hydrocarbons. *J. CO₂ Util.* **2013**, *3–4*, 102–106. [[CrossRef](#)]
56. Li, Y.; Men, Y.; Liu, S.; Wang, J.; Wang, K.; Tang, Y.; An, W.; Pan, X.; Li, L. Remarkably efficient and stable Ni/Y₂O₃ catalysts for CO₂ methanation: Effect of citric acid addition. *Appl. Catal. B Environ.* **2021**, *293*, 120206. [[CrossRef](#)]
57. Liu, Z.; Gao, X.; Liu, B.; Song, W.; Ma, Q.; Zhao, T.-s.; Wang, X.; Bae, J.W.; Zhang, X.; Zhang, J. Highly stable and selective layered Co-Al-O catalysts for low-temperature CO₂ methanation. *Appl. Catal. B Environ.* **2022**, *310*, 121303. [[CrossRef](#)]
58. Dai, Y.; Xu, M.; Wang, Q.; Huang, R.; Jin, Y.; Bian, B.; Tumorbaatar, C.; Ishtsog, B.; Bold, T.; Yang, Y. Enhanced activity and stability of Ni/La₂O₃CO₃ catalyst for CO₂ methanation by metal-carbonate interaction. *Appl. Catal. B Environ.* **2020**, *277*, 119271. [[CrossRef](#)]
59. Wierzbicki, D.; Baran, R.; Debek, R.; Motak, M.; Gálvez, M.E.; Grzybek, T.; Da Costa, P.; Glatzel, P. Examination of the influence of La promotion on Ni state in hydrotalcite-derived catalysts under CO₂ methanation reaction conditions: Operando X-ray absorption and emission spectroscopy investigation. *Appl. Catal. B Environ.* **2018**, *232*, 409–419. [[CrossRef](#)]
60. Xu, Y.; Wu, Y.; Li, J.; Wei, S.; Gao, X.; Wang, P. Combustion-impregnation preparation of Ni/SiO₂ catalyst with improved low-temperature activity for CO₂ methanation. *Int. J. Hydrogen Energy* **2021**, *46*, 20919–20929. [[CrossRef](#)]
61. Weidler, N.; Schuch, J.; Knaus, F.; Stenner, P.; Hoch, S.; Maljusch, A.; Schäfer, R.; Kaiser, B.; Jaegermann, W. X-ray Photoelectron Spectroscopic Investigation of Plasma-Enhanced Chemical Vapor Deposited NiO_x, NiO_x(OH)_y, and CoNiO_x(OH)_y: Influence of the Chemical Composition on the Catalytic Activity for the Oxygen Evolution Reaction. *J. Phys. Chem. C* **2017**, *121*, 6455–6463. [[CrossRef](#)]
62. Wu, H.; Pantaleo, G.; La Parola, V.; Venezia, A.M.; Collard, X.; Aprile, C.; Liotta, L.F. Bi- and trimetallic Ni catalysts over Al₂O₃ and Al₂O₃-MO_x (M = Ce or Mg) oxides for methane dry reforming: Au and Pt additive effects. *Appl. Catal. B Environ.* **2014**, *156–157*, 350–361. [[CrossRef](#)]
63. Cao, Y.; Li, H.; Zhang, J.; Shi, L.; Zhang, D. Promotional effects of rare earth elements (Sc, Y, Ce, and Pr) on NiMgAl catalysts for dry reforming of methane. *RSC Adv.* **2016**, *6*, 112215–112225. [[CrossRef](#)]
64. Ang, M.L.; Oemar, U.; Kathiraser, Y.; Saw, E.T.; Lew, C.H.K.; Du, Y.; Borgna, A.; Kawi, S. High-temperature water–gas shift reaction over Ni/xK/CeO₂ catalysts: Suppression of methanation via formation of bridging carbonyls. *J. Catal.* **2015**, *329*, 130–143. [[CrossRef](#)]
65. Lin, B.; Lei, Z.; Xu, F.; Cheng, N.; Mu, S. Poly(vinylpyrrolidone) tailored porous ceria as a carbon-free support for methanol electrooxidation. *Electrochim. Acta* **2018**, *290*, 55–62. [[CrossRef](#)]
66. Li, W.; Nie, X.; Jiang, X.; Zhang, A.; Ding, F.; Liu, M.; Liu, Z.; Guo, X.; Song, C. ZrO₂ support imparts superior activity and stability of Co catalysts for CO₂ methanation. *Appl. Catal. B Environ.* **2018**, *220*, 397–408. [[CrossRef](#)]
67. Gao, J.; Wang, Y.; Ping, Y.; Hu, D.; Xu, G.; Gu, F.; Su, F. A thermodynamic analysis of methanation reactions of carbon oxides for the production of synthetic natural gas. *RSC Adv.* **2012**, *2*, 2358–2368. [[CrossRef](#)]
68. Wierzbicki, D.; Moreno, M.V.; Ognier, S.; Motak, M.; Grzybek, T.; Da Costa, P.; Gálvez, M.E. Ni-Fe layered double hydroxide derived catalysts for non-plasma and DBD plasma-assisted CO₂ methanation. *Int. J. Hydrogen Energy* **2020**, *45*, 10423–10432. [[CrossRef](#)]
69. Summa, P.; Samojeden, B.; Motak, M.; Wierzbicki, D.; Alxneit, I.; Świerczek, K.; Da Costa, P. Investigation of Cu promotion effect on hydrotalcite-based nickel catalyst for CO₂ methanation. *Catal. Today* **2022**, *384–386*, 133–145. [[CrossRef](#)]
70. Wierzbicki, D.; Motak, M.; Grzybek, T.; Gálvez, M.E.; Da Costa, P. The influence of lanthanum incorporation method on the performance of nickel-containing hydrotalcite-derived catalysts in CO₂ methanation reaction. *Catal. Today* **2018**, *307*, 205–211. [[CrossRef](#)]
71. Tada, S.; Shimizu, T.; Kameyama, H.; Haneda, T.; Kikuchi, R. Ni/CeO₂ catalysts with high CO₂ methanation activity and high CH₄ selectivity at low temperatures. *Int. J. Hydrogen Energy* **2012**, *37*, 5527–5531. [[CrossRef](#)]
72. Li, L.; Zeng, W.; Song, M.; Wu, X.; Li, G.; Hu, C. Research Progress and Reaction Mechanism of CO₂ Methanation over Ni-Based Catalysts at Low Temperature: A Review. *Catalysts* **2022**, *12*, 244. [[CrossRef](#)]
73. Wang, W.; Chu, W.; Wang, N.; Yang, W.; Jiang, C. Mesoporous nickel catalyst supported on multi-walled carbon nanotubes for carbon dioxide methanation. *Int. J. Hydrogen Energy* **2016**, *41*, 967–975. [[CrossRef](#)]
74. Cai, M.; Wen, J.; Chu, W.; Cheng, X.; Li, Z. Methanation of carbon dioxide on Ni/ZrO₂-Al₂O₃ catalysts: Effects of ZrO₂ promoter and preparation method of novel ZrO₂-Al₂O₃ carrier. *J. Nat. Gas Chem.* **2011**, *20*, 318–324. [[CrossRef](#)]

75. Pan, Q.; Peng, J.; Sun, T.; Wang, S.; Wang, S. Insight into the reaction route of CO₂ methanation: Promotion effect of medium basic sites. *Catal. Commun.* **2014**, *45*, 74–78. [[CrossRef](#)]
76. Zhang, L.; Bian, L.; Zhu, Z.; Li, Z. La-promoted Ni/Mg-Al catalysts with highly enhanced low-temperature CO₂ methanation performance. *Int. J. Hydrogen Energy* **2018**, *43*, 2197–2206. [[CrossRef](#)]

Disclaimer/Publisher's Note: The statements, opinions and data contained in all publications are solely those of the individual author(s) and contributor(s) and not of MDPI and/or the editor(s). MDPI and/or the editor(s) disclaim responsibility for any injury to people or property resulting from any ideas, methods, instructions or products referred to in the content.